

# Finite Temperature Minimal Entangled Typical Thermal States Impurity Solver

Xiaodong Cao,<sup>1,\*</sup> E. Miles Stoudenmire,<sup>1</sup> and Olivier Parcollet<sup>1,2</sup>

<sup>1</sup>Center for Computational Quantum Physics, Flatiron Institute, 162 5th Avenue, New York, NY 10010, USA

<sup>2</sup>Université Paris-Saclay, CNRS, CEA, Institut de Physique Théorique, 91191, Gif-sur-Yvette, France

We present a minimally entangled typical thermal state (METTS) quantum impurity solver for general multi-orbital systems at finite temperatures. We introduce an improved estimator for the single-particle Green's function that strongly reduces the large fluctuations at long imaginary time and low temperature, which were a severe limitation of the original algorithm. In combination with the fork tensor product states ansatz, we obtain a dynamical mean field theory (DMFT) quantum impurity solver, which we benchmark for single and three-band models down to low temperatures, including the effect of spin-orbit coupling in a realistic DMFT computation for the Hund's metal Sr<sub>2</sub>RuO<sub>4</sub> down to low temperatures.

## I. INTRODUCTION

Strongly correlated materials are a central topic in condensed matter physics. Understanding or predicting their properties is a challenge that requires the development of non-perturbative quantum many-body methods. An example of such a method is the dynamical mean-field theory (DMFT), which has significantly advanced our understanding of these systems [1–7]. DMFT maps the original lattice problem into an effective impurity problem with a self-consistent bath. Solving such impurity problems remains a central computational bottleneck in the ab-initio study of strongly correlated material with DMFT.

The most common method for solving DMFT quantum impurity problems is quantum Monte Carlo (QMC) [2, 8–13]. However, its application is hindered by the intrinsic fermionic sign problem at low temperatures in many interesting cases, e.g. systems with low symmetries or spin-orbit coupling. Exact diagonalization [14–21] and numerical renormalization group [22–29] are free from the sign problem but are constrained to a small number of orbital degrees with high symmetries. Recently, matrix product states (MPS) [30–33] and its tree tensor network extensions have emerged as successful many-body wave function ansatzes for general impurity problems and have been successfully employed as impurity solvers on both real and imaginary axis [34–45]. However, these tensor network based impurity solvers are originally restricted to zero temperature calculations.

Within the tensor network framework, finite temperature computations can be conducted in two ways: *i*) the minimal entangled typical thermal states (METTS) [46–48], a Monte Carlo sampling of states with low entanglement, and *ii*) the purification method [49–52], which accounts for both thermal and quantum fluctuations by doubling the Hilbert space. Recently, a hybrid method was proposed that combines both approaches [53, 54]. It has been extended to the computation of the single-particle Green's function, in a single-orbital Anderson

impurity model [55]. However in the algorithm presented in Ref. 55, the Green's function exhibits large variance in the METTS sampling at long imaginary time (i.e. for  $\tau \sim \beta/2$ ), which severely limits the capabilities of the method as an impurity solver at low frequencies.

In this work, we show how to reduce this variance significantly using an improved estimator for Green's function. Combined with the fork tensor product state many-body wave function ansatz, we obtain an impurity solver for general impurity problems at finite temperatures, which we show to be efficient for three band systems, down to very low temperatures, even in the presence of spin-orbit coupling (SOC).

The paper is organized as follows. In Sec. II, we introduce our improved estimator for the computation of the imaginary time Green's function in the hybrid METTS/purification method. In Sec. III A, we use single-band benchmarks to demonstrate the efficiency of the improved estimator with excellent agreement on the self-energy. In Sec. III B, we apply our method to a realistic DMFT study of Sr<sub>2</sub>RuO<sub>4</sub> and show the effect of SOC in parameter regimes that are inaccessible to QMC algorithms. Finally, we conclude in Sec. IV.

## II. METTS IMPROVED ESTIMATOR FOR IMAGINARY TIME GREEN'S FUNCTIONS

We consider a multiorbital Anderson impurity model coupled to a finite bath defined by

$$\begin{aligned}\hat{H} &= \hat{H}_{\text{loc}} + \hat{H}_{\text{bath}}, \\ \hat{H}_{\text{loc}} &= \sum_{\alpha} \varepsilon_{\alpha_1 \alpha_2} \hat{d}_{\alpha_1}^{\dagger} \hat{d}_{\alpha_2} + \sum_{\alpha} U_{\alpha_1 \alpha_2 \alpha_3 \alpha_4} \hat{d}_{\alpha_1}^{\dagger} \hat{d}_{\alpha_2}^{\dagger} \hat{d}_{\alpha_3} \hat{d}_{\alpha_4}, \\ \hat{H}_{\text{bath}} &= \sum_{i=1}^{N_b} \left( \sum_{\kappa} \epsilon_{\kappa}^i \hat{c}_{i,\kappa}^{\dagger} \hat{c}_{i,\kappa} + \sum_{\kappa \alpha} V_{\alpha \kappa}^i \hat{d}_{\alpha}^{\dagger} \hat{c}_{i,\kappa} + h.c. \right)\end{aligned}\quad (1)$$

where  $\hat{H}_{\text{bath}}$  is the bath,  $\hat{H}_{\text{loc}}$  is the local impurity with its interactions, including the Coulomb interaction  $U_{\alpha_1 \alpha_2 \alpha_3 \alpha_4}$  and various intra-site effects  $\varepsilon_{\alpha_1 \alpha_2}$ . Here,  $\alpha$  (resp.  $\kappa$ ) denotes the spin and orbital degrees of freedom of the impurity (resp. bath);  $i$  is the bath site index, and  $N_b$

\* xcao@flatironinstitute.org

is the number of bath sites per spin-orbital. In this Hamiltonian representation, the hybridization function reads

$$\Delta_{\alpha_1\alpha_2}(i\omega_n) = \sum_{i=1}^{N_b} \sum_{\kappa} \frac{V_{\alpha_1\kappa}^i V_{\alpha_2\kappa}^{i*}}{i\omega_n - \epsilon_{\kappa}^i}, \quad (2)$$

In the context of DMFT computation, where the hybridization function  $\Delta$  is the input of the impurity solver,  $\Delta$  is fitted to the finite bath form of Eq. (2) using a standard procedure presented in Appendix A.

### A. METTS and Purification

The central quantity in solving DMFT self-consistency equations is the single-particle Green's function, defined as

$$\begin{aligned} G_{\alpha_1\alpha_2}(\tau) &= -\langle \mathcal{T} \hat{d}_{\alpha_1}(\tau) \hat{d}_{\alpha_2}^\dagger \rangle \\ &= -\frac{1}{\mathcal{Z}} \sum_i \langle i | e^{-\beta \hat{H}} \mathcal{T} \hat{d}_{\alpha_1}(\tau) \hat{d}_{\alpha_2}^\dagger | i \rangle, \end{aligned} \quad (3)$$

where  $\beta = 1/T$  denotes the inverse temperature,  $\mathcal{T}$  is the time ordering operator and  $\mathcal{Z} = \sum_i \langle i | e^{-\beta \hat{H}} | i \rangle$  is the partition function. The states  $\{|i\rangle\}$  represent a complete and orthonormal basis. Using the cyclic property of the trace, the Green's function can be rewritten for  $\tau > 0$  as

$$\begin{aligned} G_{\alpha_1\alpha_2}(\tau) &= -\frac{1}{\mathcal{Z}} \sum_i \langle i | e^{-\beta \hat{H}/2} \hat{d}_{\alpha_1}(\tau) \hat{d}_{\alpha_2}^\dagger e^{-\beta \hat{H}/2} | i \rangle \\ &= -\frac{1}{\mathcal{Z}} \sum_i p(i) \langle \phi_i | \hat{d}_{\alpha_1}(\tau) \hat{d}_{\alpha_2}^\dagger | \phi_i \rangle, \end{aligned} \quad (4)$$

defining the normalized states  $|\phi_i\rangle \equiv e^{-\beta \hat{H}/2} |i\rangle / \sqrt{p(i)}$  and the probability  $p(i) \equiv \langle i | e^{-\beta \hat{H}} | i \rangle$ .

When  $\{|i\rangle\}$  are chosen to be unentangled states,  $|\phi_i\rangle$  are minimally entangled typical thermal states or ‘‘METTS’’ and  $p(i)$  is the unnormalized probability weight of each METTS [46, 47]. In general, a METTS  $|\phi_i\rangle$  is a many-body state whose entanglement grows smoothly from zero at smaller  $\beta$ . For large  $\beta$ , each METTS approaches the ground state. METTS states can be importance sampled using an algorithm where each METTS is ‘‘collapsed’’ into a product state that generates the next METTS [46, 47]. Thus the METTS approach is a quantum Monte Carlo algorithm involving entangled rather than classical configurations.

To represent each METTS wavefunction, we adopt a tensor network with a ‘‘fork’’ structure, where each interacting impurity site has its own separate chain of bath degrees of freedom attached to it. Such a fork tensor product state ansatz has been demonstrated to efficiently capture the entanglement structure of states of multi-orbital models [43, 45, 56]. To perform the imaginary time evolution necessary to construct each METTS, we

use the time-dependent variational principle (TDVP) combined with a global basis expansion [45, 57–60], which has been demonstrated capable of providing highly accurate results for impurity problems. Tensor operations are implemented using the ITensor library [61, 62]. Further implementation details can be found in Appendix B.

A possible drawback of the METTS approach is that it can require a large number of samples to achieve desirable precision. One method that has been proposed to reduce the number of samples is to ‘‘purify’’ a subset of the sites of the initial state generating each METTS [53–55]. To purify a site, one introduces a new corresponding ‘‘ancilla’’ site and prepares the purified site to be maximally entangled with the ancilla site before time-evolving the state, i.e.,

$$|i\rangle = \bigotimes_{x \in I_p} \left[ \frac{1}{\sqrt{2}} (|0\rangle_{P_x} |1\rangle_{A_x} + |1\rangle_{P_x} |0\rangle_{A_x}) \right] \bigotimes_{y \notin I_p} |s_y\rangle,$$

where  $I_p$  represents the set of purified site indices.  $P_x$  and  $A_x$  subscripts indicate the physical and auxiliary degrees of freedom of site  $x$ , respectively.  $|s_y\rangle \in \mathcal{H}_y \equiv \{|0\rangle_y, |1\rangle_y\}$  is a state in the local Hilbert space of site  $y$ , where  $|0\rangle_y$  and  $|1\rangle_y$  denote the empty and occupied state, respectively. In the limit of purifying all of the sites, only a single sample would be required. This limit is known as the ‘‘purification method’’, and while requiring no sampling, it has a rather high cost in the low-temperature limit.

The optimal choice of which and how many sites to purify turns out to be delicate and model dependent, as detailed in Refs. 53 and 55, and one aims to balance a reduction in the number of samples against an increase in the growth of entanglement. A more detailed discussion on the dependence of the sampling efficiency and bond dimension growth on the number of purified sites,  $N_p$ , is presented in Appendix D. In this work, we choose to purify the bath sites that fluctuate most by purifying the first  $N_p$  bath sites which have the lowest absolute on-site potential  $|\epsilon^i|$ , while keeping impurity degrees of freedom unpurified. With this purification scheme, we anticipate sampling primarily the impurity degrees of freedom, as fluctuations related to the bath degrees of freedom are mainly addressed through purification.

### B. Improved Estimator

By generating a sufficiently large number of  $N_S$  samples through Monte Carlo sampling as described above, the Green's function  $G_{\alpha_1\alpha_2}(\tau)$  in Eq. (3) can be computed as the average of estimators measured on each sample  $i$  as

$$\begin{aligned} G_{\alpha_1\alpha_2}(\tau) &= \frac{1}{N_S} \sum_{i=1}^{N_S} \begin{cases} g_{\alpha_1\alpha_2}^{i>}(\tau), & \text{for } 0 \leq \tau \leq \beta/2, \\ g_{\alpha_1\alpha_2}^{i<}(\tau), & \text{for } \beta/2 \leq \tau \leq \beta, \end{cases} \\ g_{\alpha_1\alpha_2}^{i>}(\tau) &\equiv -\langle \phi_i | \hat{d}_{\alpha_1}(\tau) \hat{d}_{\alpha_2}^\dagger | \phi_i \rangle, \\ g_{\alpha_1\alpha_2}^{i<}(\tau) &\equiv -\langle \phi_i | \hat{d}_{\alpha_2}^\dagger \hat{d}_{\alpha_1}(\tau - \beta) | \phi_i \rangle. \end{aligned} \quad (5)$$

Here,  $g_{\alpha_1\alpha_2}^{i>}(\tau)$  and  $g_{\alpha_1\alpha_2}^{i<}(\tau)$  are referred to as the greater and lesser estimator, respectively. The splitting of the estimator into  $g_{\alpha_1\alpha_2}^{i>}(\tau)$  for  $\tau \leq \beta/2$  and  $g_{\alpha_1\alpha_2}^{i<}(\tau)$  for  $\tau > \beta/2$  serves to prevent the overflow of the norm during the imaginary time evolution and reduce the computational cost by reusing states generated during calculating  $|\phi_i\rangle$  [55].

However, as observed in Ref. 55 and as shown in Fig. 1(a)(c), the above estimators exhibit significant variance as  $\tau$  approaches  $\beta/2$ . This large variance arises from a mismatched importance sampling between the METTS states  $|\phi_i\rangle$  sampled at a temperature  $\beta$  and the overlaps of the states  $[\langle\phi_i|\hat{d}_{\alpha_1}(\tau)\rangle[\hat{d}_{\alpha_2}^\dagger|\phi_i\rangle]]$  or  $[\langle\phi_i|\hat{d}_{\alpha_2}^\dagger(\tau)\rangle[\hat{d}_{\alpha_1}(\tau-\beta)|\phi_i\rangle]]$  which are not necessarily small when the probabilities  $p(i)$  are small.

In order to mitigate this issue, we rewrite the decomposition of  $G$  differently. Using the notation  $\tilde{\tau} = \beta - \tau$ , we introduce *improved estimators*  $\bar{g}$  such that

$$G_{\alpha_1\alpha_2}(\tau) = \frac{1}{N_S} \sum_{i=1}^{N_S} \begin{cases} \bar{g}_{\alpha_1\alpha_2}^{i>}(\tau), & \text{for } 0 \leq \tau \leq \beta/2, \\ \bar{g}_{\alpha_1\alpha_2}^{i<}(\tilde{\tau}), & \text{for } \beta/2 \leq \tau \leq \beta \end{cases}$$

$$\bar{g}_{\alpha_1\alpha_2}^{i>}(\tau) \equiv -\langle\phi_i^{(\beta-\tau)}|\hat{d}_{\alpha_1}e^{-\frac{\tau\hat{H}}{2}}e^{-\frac{\tau\hat{H}}{2}}\hat{d}_{\alpha_2}^\dagger|\phi_i^{(\beta-\tau)}\rangle, \quad (6)$$

$$\bar{g}_{\alpha_1\alpha_2}^{i<}(\tilde{\tau}) \equiv -\langle\phi_i^{(\beta-\tilde{\tau})}|\hat{d}_{\alpha_2}^\dagger e^{-\frac{\tilde{\tau}\hat{H}}{2}}e^{-\frac{\tilde{\tau}\hat{H}}{2}}\hat{d}_{\alpha_1}|\phi_i^{(\beta-\tilde{\tau})}\rangle,$$

$$|\phi_i^{(\tau)}\rangle \equiv \frac{e^{-\frac{\tau\hat{H}}{2}}|i\rangle}{\sqrt{\langle i|e^{-\beta\hat{H}}|i\rangle}}.$$

We provide evidence in the next section that these improved estimators strongly reduce the variance problem near  $\tau = \beta/2$ . They also has a natural particle hole symmetry. Furthermore, the maximal evolved time in this new scheme is  $\beta/2$ , as opposed to  $\beta$  of the original estimator—a difference that might be computationally significant for models with highly entangled low-temperature or ground state physics. The drawback of the improved estimators is that they require one to compute  $g_{\alpha_1\alpha_2}^{i\leq}(\tau)$  at each  $\tau$  point separately. Nevertheless, this issue is strongly mitigated by the use of the compact discrete Lehmann representation (DLR) of the Green's function [63]. The DLR approach allows the Green's function on the whole imaginary time grid to be efficiently represented to high precision by merely computing its values on a modest number of special  $\tau$  points making up the ‘‘DLR grid’’, whose number grows only logarithmically with the inverse temperature.

### III. RESULT AND DISCUSSION

In this section, we first present a benchmark of the improved estimator and then apply the METTS algorithm method to the archetypical Hund's metal  $\text{Sr}_2\text{RuO}_4$ . The appendices present additional material, such as: detailed discussions on the number of bath sites and purified sites are presented in Appendix C and D; benchmark of

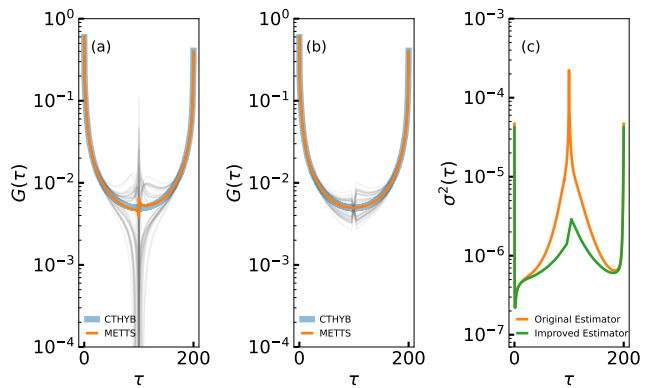


Fig. 1. The single-particle Green's function of DMFT solution of the single-orbital Hubbard model from (a) the original estimator and (b) the improved estimator at  $\beta D = 400$ . The cyan line is the CTHYB quantum Monte Carlo result, using the implementation Ref. 64, and the grey lines are the estimators measured on each sample. (c) The METTS variance defined in Eq. (7) of the original estimator (orange line) and improved estimator (green line). In both cases,  $N_S = 240$ ,  $N_p = 4$  and  $N_b = 8$ .

the method against the continuous-time hybridization expansion quantum Monte Carlo algorithm (CTHYB) for a three-band Kanamori model in Appendix E, with an excellent agreement of the self-energy down to very low temperature  $\beta D = 800$  (where  $D$  is the half-bandwidth).

#### A. Improved Estimator

We first investigate the effect of the improved estimator on the large fluctuations observed in the previous METTS computation around  $\tau = \beta/2$  [55]. We consider the DMFT solution of a single-band Hubbard model on the Bethe lattice with a filling of  $n = 0.8$  and an interaction strength of  $U = 4D$ , where  $D$  denotes the half-bandwidth of the semielliptic density of states.

In Fig. 1, we show the Green's function as a function of imaginary time  $\tau$  measured from the original estimator on panel a) and improved estimator on panel b). When employing the original estimator, our benchmarks are in excellent agreement with the CTHYB quantum Monte Carlo results using the implementation in the TRIQS software [64, 65] across the entire imaginary time domain, except for  $\tau \approx \beta/2$  due to large fluctuations in the METTS sampling, as discussed previously [55]. As shown in Fig. 1(b), the large variance close to  $\beta/2$  is strongly reduced with the improved estimator. In order to quantify this effect, we consider the METTS variance defined as

$$\sigma^2(\tau) \equiv \frac{1}{N_S} \sum_{i=1}^{N_S} \|g^i(\tau) - G(\tau)\|^2. \quad (7)$$

where  $g$  is the estimator and  $G$  its average over the  $N_S$  samples. In Fig. 1(c), we indeed see that the improved

estimator significantly reduces the variance around  $\beta/2$ .

## B. Application to Sr<sub>2</sub>RuO<sub>4</sub>

Let us now consider Sr<sub>2</sub>RuO<sub>4</sub> [66], within the DMFT framework. In addition to the still-debated unconventional superconducting state below  $\sim 1.5$  K [67, 68], the normal state, including the Hund's metal state [7, 69] and Fermi liquid state below  $T_{\text{FL}} \approx 25$  K [28, 66], has attracted considerable attention. Previous DMFT studies have been successfully applied to explain various experimental observations, such as mass enhancement [70, 71], static magnetic responses [72], and the enhancement of spin-orbital coupling strength by a factor of two due to correlation effects [44, 73]. Due to the availability of results with multiple methods (CTHYB, NRG), this material is an excellent benchmark for multiorbital quantum impurity solvers in a realistic DMFT setup.

The low-energy physics of Sr<sub>2</sub>RuO<sub>4</sub> is determined by the Ru  $4d$ - $t_{2g}$  orbitals hybridizing with oxygen  $2p$  orbitals [7, 74]. A minimal one-body Hamiltonian can be constructed by considering the three maximally localized  $t_{2g}$  orbitals, which are obtained from the DFT Kohn-Sham orbitals without spin-orbit coupling [75–77]. The noninteracting density of states of Sr<sub>2</sub>RuO<sub>4</sub> consists of a quasi-two-dimensional  $d_{xy}$  band and two degenerate quasi-one-dimensional  $d_{yz/xz}$  bands. Notably, the  $d_{xy}$  band exhibits a van Hove singularity slightly above the Fermi energy, while its spectral function features a long tail below the Fermi energy and a relatively larger bandwidth than the  $d_{xz/yz}$  bands. The latter bands display typical quasi-one-dimensional characteristics with singularities located at their edges [74]. The Coulomb interaction takes the Kanamori form as

$$\hat{H}_{\text{K}} = \frac{1}{2}(U - 3J)\hat{N}(\hat{N} - 1) + \frac{5}{2}J\hat{N} - 2J\hat{S}^2 - \frac{1}{2}J\hat{L}^2, \quad (8)$$

with  $U = 2.3$  eV and  $J = 0.4$  eV [28, 73, 78]. Here  $\hat{N}$ ,  $\hat{L}$ , and  $\hat{S}$  are the total particle number, orbital, and spin momentum operators of the impurity, respectively. The SOC term in the Hamiltonian reads

$$\hat{H}_{\text{soc}} = i\frac{\lambda}{2} \sum_{mm'm''} \zeta_{mm'm''} \sum_{\sigma\sigma'} d_{m\sigma}^\dagger d_{m'\sigma'} \tau_{\sigma\sigma'}^{m''}, \quad (9)$$

where  $\zeta$  is the completely antisymmetric tensor and  $\boldsymbol{\tau}$  the Pauli vector. An isotropic coupling constant of  $\lambda = 0.11$  eV is chosen for this term, with  $m \in \{d_{xy}, d_{yz}, d_{xz}\}$  and  $\sigma \in \{\uparrow, \downarrow\}$ . We use  $N_b = 8$ ,  $N_p = 4$  for calculations without SOC, and  $N_b = 6$ ,  $N_p = 2$  with SOC. In every calculation, the measurements are averaged over  $N_S = 1080$  samples, with each sample calculated using a maximal bond dimension of  $m = 240$  and a truncation error cutoff of  $t_w = 10^{-10}$ . Due to the local  $D_{4h}$  point group of Ru atoms, we omit the spin index when presenting results without SOC.

We start with results without SOC. In Fig. 2, we compare the real (upper panels) and imaginary (lower panels) parts of the DMFT self-energy obtained from our approach with CTHYB quantum Monte Carlo at three temperatures, located in the fully incoherent ( $T = 464$ K), crossover ( $T = 116$ K), and coherent ( $T = 29$ K) regions [70]. We observe excellent agreement between our results and CTHYB at these three typical temperatures, demonstrating the accuracy of our method.

Our approach's capability to provide accurate results across large temperature range is further demonstrated by comparing the extracted quasiparticle weight  $Z = (1 - \partial_{\omega_n} \text{Im}\Sigma(i\omega_n)|_{\omega_n \rightarrow 0})^{-1}$  from our method with CTHYB in Fig. 3(a) [79]. We observe excellent agreement for temperatures as high as  $T = 464$  K down to low temperatures as  $T = 29$  K, which is close to the Fermi-liquid temperature  $T_{\text{FL}} \approx 25$  K [28, 66]. Notably, accurately calculating the first few Matsubara frequencies of the self-energy can be challenging for CTHYB at very low temperatures. Our method, however, benefiting from fork tensor product state representation of the impurity wave function, is less constrained by low-temperature calculations and can access even lower one as  $T = 23.2$  K.

Fig. 3(b) and (c) depict the imaginary part of the self-energy of the  $d_{xy}$  and  $d_{yz/xz}$  orbitals. For  $T = 23.2$  K, we observe a linear behavior of  $\text{Im}\Sigma(i\omega_n)$  as  $\omega_n \rightarrow 0$  for all three orbitals, indicating Fermi liquid behavior. The quasiparticle weight extracted at  $T = 23.2$  K is 0.18 for the  $d_{xy}$  orbital and 0.28 for the  $d_{yz/xz}$  orbitals, in good agreement with previous calculations [28, 73] and experimental results [66, 71]. Despite the larger bandwidth of the  $d_{xy}$  orbital, its quasiparticle excitations are more renormalized than the  $d_{yz/xz}$  orbitals. This unexpected behavior can be attributed to the relatively smaller spectral weight of the hybridization function for the  $d_{xy}$  orbital near the Fermi energy due to the van Hove singularity [70].

Let us now turn to computations with SOC. This term is known to play a significant role in this material, although it is only a few percent of the bandwidth, its inclusion is crucial for accurately describing the experimental Fermi surface [45, 71, 74]. Incorporating SOC is particularly challenging for QMC solvers, with calculations performed only for temperatures above 200 K [73, 78, 80]. While zero-temperature results are available from MPS-based solvers, using an artificial inverse temperature of  $\beta^{\text{eff}} = 200$  eV<sup>-1</sup> [44], the impact of SOC at intermediate temperatures on single-particle quantities remains to be explored with a direct computation. Here, we present results with SOC at  $T = 58$  K. In Fig. 4, we compare  $\text{Im}\Sigma(i\omega_n)$  with (filled circles) and without (open circles) SOC at  $T = 58$  K. As anticipated, the diagonal elements are only slightly modified, and the quasiparticle weights slightly change from 0.226 to 0.228 for the  $d_{xy}$  orbital and from 0.301 to 0.306 for the  $d_{yz/xz}$  orbitals. As depicted in the inset, the effective in and out-of-plane spin-orbital coupling strengths respectively defined as

$$\lambda_{xy}^{\text{eff}}(i\omega_n) \equiv \lambda - 2\text{Im}\Sigma_{xy\uparrow, xz\downarrow}(i\omega_n), \quad (10a)$$

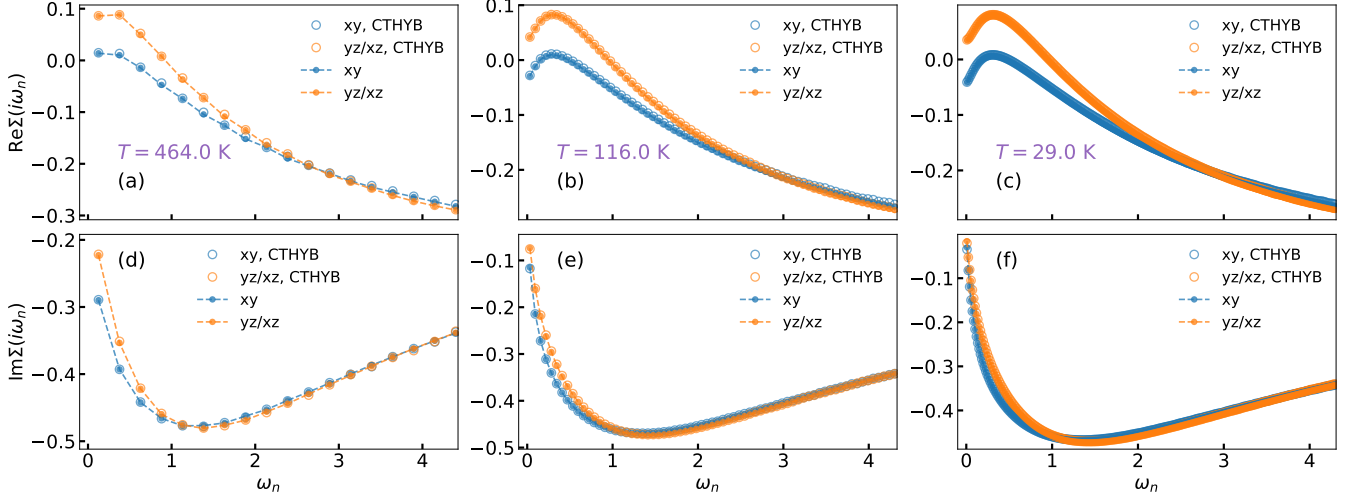


Fig. 2. Comparison of the real (a-c) and imaginary (d-f) parts of the DMFT self-energy of  $\text{Sr}_2\text{RuO}_4$  without spin-orbit coupling, calculated using the METTS solver (full circles) and CTHYB quantum Monte Carlo (open circles) at  $T = 464$  K (left panels),  $T = 116$  K (middle panels), and  $T = 29$  K (right panels).

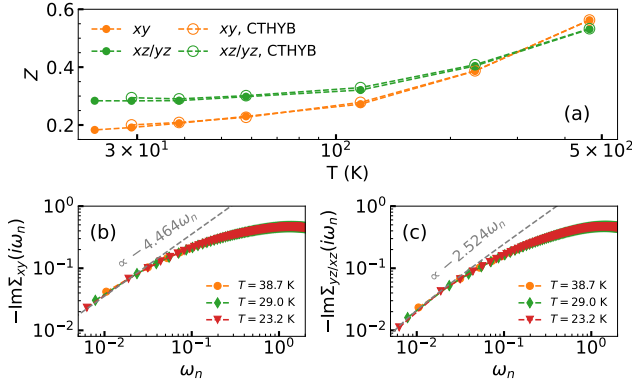


Fig. 3. (a) Comparison of quasiparticle weights  $Z$  from our approach (filled circles) and CTHYB quantum Monte Carlo (open circles) at various temperatures. (b) Imaginary part of the DMFT self-energy for the  $d_{xy}$  orbital and (c) the two degenerate  $d_{yz}$  and  $d_{xz}$  orbitals at temperatures of  $T = 38.7$  K (orange circles),  $T = 29.0$  K (green diamonds), and  $T = 23.2$  K (red triangles). The dashed grey lines serve as guides to the eye and are linear with respect to  $\omega_n$ .

$$\lambda_z^{\text{eff}}(i\omega_n) \equiv \lambda + 2\text{Im}\Sigma_{yz\uparrow, xz\uparrow}(i\omega_n) \quad (10b)$$

are essentially frequency-independent over a wide frequency range and can be considered as constant single-particle terms added to the bare ones. This enhancement of SOC strength by correlation effects, resulting in  $\lambda_{xy}^{\text{eff}} \approx 0.19$  eV and  $\lambda_z^{\text{eff}} \approx 0.2$  eV, lifts the degeneracies at the crossing along the Brillouin zone and gives rise to well-separated sheets, consistent with experimental observations [71]. The originally isotropic atomic SOC now exhibits some anisotropy between the in- and out-of-plane values due to the lower-symmetry local point group

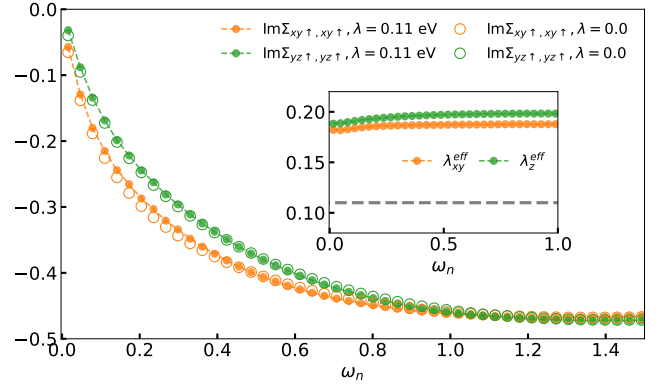


Fig. 4. Comparison of the imaginary part of selected self-energy components for  $\text{Sr}_2\text{RuO}_4$  with (filled circles) and without (open circles) spin-orbit coupling at  $T = 58$  K. The inset illustrates the effective spin-orbit coupling strength  $\lambda_{xy}^{\text{eff}}$  (orange) and  $\lambda_z^{\text{eff}}$  (green). The grey dashed line represents the bare coupling strength of  $\lambda = 0.11$  eV.

$D_{4h}$  of the Ru ion. These findings are in agreement with earlier finite temperature CTHYB calculations [73, 81] and zero-temperature MPS calculations [28, 44].

#### IV. CONCLUSION

In summary, we have introduced an improved estimator for Green's function in METTS computations. Using this estimator significantly reduces the variance in certain time ranges where the previous estimator of Ref. [55] would require many more samples. Combining the METTS and purification approach with the fork tensor product

state network, we obtained a finite-temperature quantum impurity solver which works for three-band systems at low temperature, even in the presence of spin-orbit coupling, a regime inaccessible to the quantum Monte Carlo methods. We illustrated our method with a computation of the self-energy for  $\text{Sr}_2\text{RuO}_4$  including the spin-orbit coupling.

Because both the improved  $G(\tau)$  estimator and the METTS algorithm are quite general purpose, we expect the above improvements to be useful for studying strongly-correlated lattice models where METTS has already been used to compute thermodynamic properties [82–84]. Having controlled access to the imaginary-time Green’s function should help to understand scenarios such as the disordered intermediate- $U$  phase of the triangular lattice Hubbard model [83].

## ACKNOWLEDGMENTS

The Flatiron Institute is a division of the Simons Foundation.

### Appendix A: Fit of the hybridization function

In this section, we give the details of our fitting procedure of the hybridization function to the form Eq.(2). For a given hybridization function  $\Delta$ , the parameters  $\epsilon$  and  $V$  are determined by minimizing a cost function [3]

$$\chi(\{\epsilon, V\}) = \frac{1}{N_{\text{fit}}} \sum_{n=0}^{N_{\text{fit}}} \frac{1}{\omega_n^\gamma} \|\Delta(i\omega_n) - \bar{\Delta}(i\omega_n)\|, \quad (\text{A1})$$

where  $\omega_n$  are Matsubara frequencies,  $N_{\text{fit}} = 1500$  in this paper and  $\|\cdot\|$  is the Frobenius norm. The parameter  $\gamma \in [0, 1]$  adjusts the weighting of low frequencies in the cost function  $\chi$ . For  $\gamma = 0$ , all frequencies are treated equally, while low frequencies are assigned greater weight for  $\gamma > 0$ . We found that choosing  $\gamma = 1$  stabilizes our DMFT convergence, particularly in cases where a small number of bath sites  $N_b$  is used.

### Appendix B: Implementation and Computational details

In this appendix, we elaborate on the implementation and computational details of the METTS solver. To calculate each  $g_{\alpha_1\alpha_2}(\tau)$ , one first evolves a product state  $|i\rangle$  in imaginary time to  $|\phi_i\rangle = e^{-\beta\hat{H}/2} |i\rangle / \sqrt{\langle i| e^{-\beta\hat{H}} |i\rangle}$ . Due to the non-local nature of the impurity Hamiltonian and the absence of direct interaction between the bath degrees of freedom, the two-site TDVP cannot adjust the bond dimension during an imaginary time evolution. Therefore, one can either employ an alternative time evolution method, such as the global Krylov time evolution method,

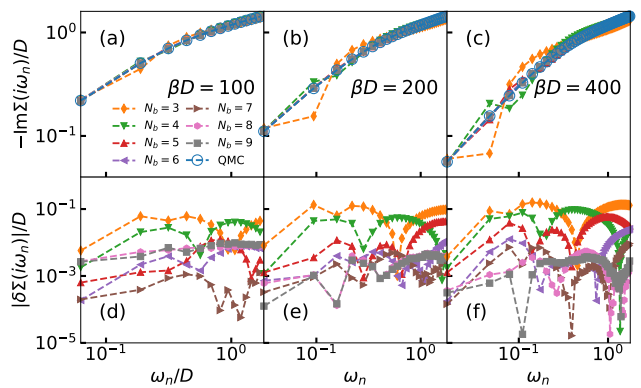


Fig. C.1. (a)-(c) Imaginary part of the self-energy, and (d)-(f) corresponding differences compared to QMC results, for DMFT solution of the single-band model at a filling of  $n = 0.8$  and interaction strength  $U = 4D$ . Results are obtained with varying numbers of bath sites ( $N_b = 3, 4, 5, 6, 7, 8$  and  $9$ ) per spin-orbital. Panels are organized by temperature:  $\beta D = 100.0$  (left),  $\beta D = 200.0$  (middle), and  $\beta D = 400.0$  (right).

during the initial time steps, and then switch to either two-site or single-site TDVP up to  $\beta/2$ . In our implementation, we extend the global basis expansion method proposed in [60] for MPS to fork tensor product states. In each of the time evolution steps,  $|\psi(\tau + \Delta\tau)\rangle = e^{-\Delta\tau\hat{H}} |\psi(\tau)\rangle$ , a series of  $N_k$  reference states are generated as

$$\left\{ \left(1 - \Delta\tau\hat{H}\right) |\psi(\tau)\rangle, \dots, \left(1 - \Delta\tau\hat{H}\right)^k |\psi(\tau)\rangle \right\},$$

and used to expand the basis of  $|\psi(\tau)\rangle$ . In general, the sequential application of  $\left(1 - \Delta\tau\hat{H}\right)$  onto an fork tensor product state increases the bond dimension rapidly and is computationally expensive. However, since high accuracy is not required for each reference state for basis expansion, we truncate these reference states with a relatively small bond dimension of around  $m' = 50$ . Moreover, we find that in all our calculations, a relatively small  $N_k = 1, 2$  is typically sufficient.

For calculating each METTS state, we employ an exponential growth imaginary time grid as  $\{\tau_0\Delta\tau^0, \tau_0\Delta\tau^1, \tau_0\Delta\tau^2, \dots, \beta/2\}$ , which ensures a small time step at the beginning of the imaginary time evolution, while increasing the time steps as approaching  $\beta/2$ . Such an exponential time grid has been demonstrated to speed up calculations exponentially and provide better accuracy [85]. In our implementation, we have  $\tau_0 = 0.05$ , and  $\Delta\tau$  is determined by a given number of imaginary time points  $N_\tau$ , which is set according to  $\beta$ . For instance, for the  $\text{Sr}_2\text{RuO}_4$  calculations, we have  $N_\tau = 4\beta/5$ .

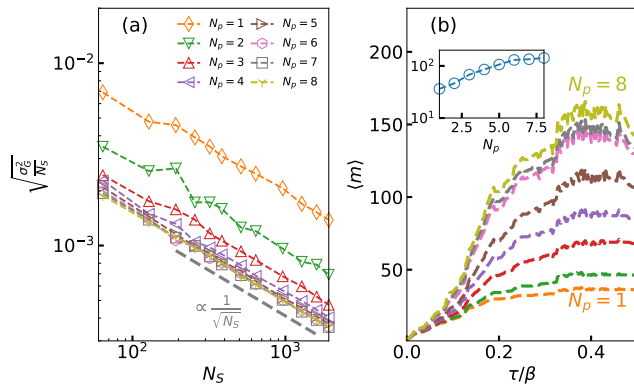


Fig. D.1. (a) Standard error of the mean  $\sqrt{\sigma_G^2/N_S}$  as a function of Monte Carlo sampling size  $N_S$  for various numbers of purified bath sites  $N_p$  per spin-orbital in the DMFT solution of the single-band Hubbard model. The dashed grey line represents a guide to the eye and is proportional to  $1/\sqrt{N_S}$ . (b) Monte Carlo sample, as a function of imaginary time  $\tau$  with various  $N_p$  values, and the insert shows  $\langle m \rangle$  at  $\tau = \beta/2$  as a function of  $N_p$ . The calculations are performed with  $N_b = 8$  at  $\beta D = 200$  and a truncation weight of  $t_w = 10^{-11}$  for the time evolution.

### Appendix C: Bath size dependence

Although the convergence of DMFT solutions from an impurity solver employing finite bath sites toward the continuous limit has been extensively discussed [3, 86–88], for completeness, we present our solver's results at various temperatures and bath sites in Fig. C.1 for the single-band model same as Sec. III A in main text. As  $N_b$  ranges from 3 to 7, we observe a systematic convergence of  $\Sigma(i\omega_n)$  to the QMC continuous limit. Comparing panels (a) and (c), we find that lower temperatures ( $\beta D = 400$ ) require larger  $N_b \geq 6$  to achieve satisfactory agreement with QMC results, unlike cases at higher temperatures ( $\beta D = 100$ ) showing excellent agreement with QMC already with  $N_b = 4$ . For  $\beta D = 200$  and 400, increasing  $N_b$  further from 8 to 9 no longer yields substantial improvements, and for  $\beta D = 100$ , we encounter the "over-fitting" problem for  $N_b = 8, 9$  as indicated by the increase of error  $\delta\Sigma(i\omega_n)$  in Fig. C.1(d).

### Appendix D: Purification versus sampling. Role of $N_p$

Here we discuss the role of  $N_p$ , the number of purified sites, using the single-band model same as Sec. III A in the main text. In Fig. D.1(a), we present the imaginary time integrated variance

$$\sigma_G^2 = \int_0^\beta \sigma^2(\tau) d\tau \quad (\text{D1})$$

as a function of the number of samples  $N_S$  for increasing  $N_p$ . We see that increasing  $N_p$  from 1 to 4 strongly

reduces the METTS fluctuations. For  $N_p \geq 4$ , this reduction is much more modest, and the standard error of the mean,  $\sqrt{\sigma_G^2/N_S}$ , starts to follow a clear standard  $1/\sqrt{N_S}$  decay rate, characteristic of Monte Carlo sampling. In Fig. D.1(b), we show the averaged maximal bond dimension  $\langle m \rangle$  versus  $\tau$ , for various  $N_p$ . As expected, the bond dimension grows with  $N_p$ , and with imaginary time  $\tau$ . The growth with  $\tau$  tends to saturate, due to the fact that  $|\phi_i\rangle$  converges to the ground state in the  $\beta \rightarrow \infty$  limit. We also observe that as  $N_p \rightarrow N_b$ , the average bond dimension increases more slowly: the purification of the bath sites far away from Fermi level has little effect, probably due to their fillings being very close to 0 and 1. We conclude that, for these parameters, there is actually an optimum in  $N_p$  around  $N_p \approx 4$  above which the computational cost of forming each METTS (measured by the average bond dimension) continues to grow with  $N_p$ , while the METTS variance does not decrease significantly anymore.

### Appendix E: Benchmark: three-band model

In this appendix, we benchmark our approach on a three-band model. We consider a Kanamori Hamiltonian of form Eq. (8) in the main text. Each impurity orbital is separately coupled to a bath with an identical semielliptic density of states of half-bandwidth of  $D$ . We use a filling of  $\langle \hat{N} \rangle = 2$ , and interaction strengths of  $U = 4D$  and  $J = U/6$ .

In Fig. E.1(a)-(h), we see that the DMFT self-energy  $\Sigma(i\omega_n)$  obtained with our method is in very good agreement with CTHYB at various temperatures. The precise low-frequency dependency of the self-energy constitutes a more rigorous benchmark of the method. In this "Hund's metal" model, the strong suppression of Kondo screening scales by Hund's coupling gives rise to a phase characterized by an almost frozen local spin moment and a power-law behavior in the low-frequency self-energy, in contrast to ordinary Fermi-liquid behavior [7, 89, 90]. This behaviour is illustrated in Fig. E.1(i): the self-energy exhibits a  $\Sigma(i\omega_n)/D \sim (\omega_n/D)^{0.5}$  power-law behavior at low frequencies. For the lower temperature case of  $\beta D = 800$ , a crossover to Fermi-liquid behavior is observed, indicated by the linear dependence of the self-energy on  $\omega_n/D$  at low frequencies.

In Fig. E.2, we show the convergence of self-energy with respect to bond dimension at various temperatures for the three-band model. We observe a systematical convergence of the self-energy with increasing  $m$ . The low frequencies are more sensitive to the bond dimension. For  $\beta D = 100$ ,  $m = 80$  is enough to achieve a satisfactory accuracy, while for  $\beta D = 800$ , a larger bond dimension of  $m = 200$  is required.

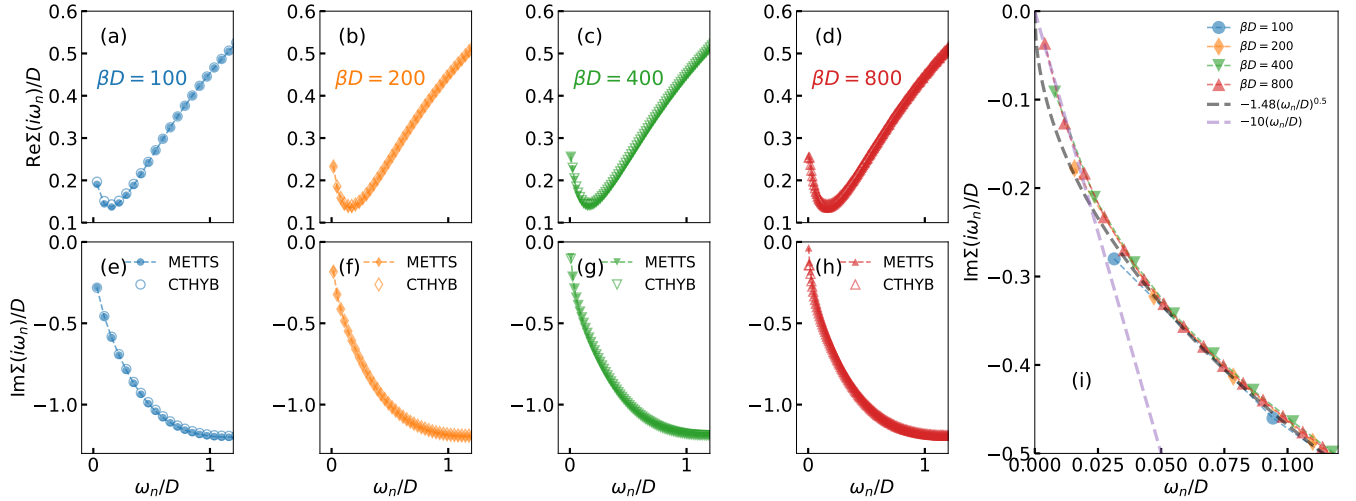


Fig. E.1. Comparison of (a-d) real and (e-h) imaginary part of DMFT self-energy for the degenerate three-orbital model using the METTS solver (filled symbols) with CTHYB results (open symbols) at various temperatures. (i) Imaginary part of the self-energy as a function of Matsubara frequency at various temperatures. Dashed grey and purple lines indicate the scaling behavior of  $\omega_n^{0.5}$  and  $\omega_n$ , respectively. For all METTS calculations, we use  $N_b = 8$  bath sites per spin-orbital, out of which  $N_p = 5$  are purified. The number of Monte Carlo samples is  $N_S = 500$ , and the bond dimension is  $m = 200$ .

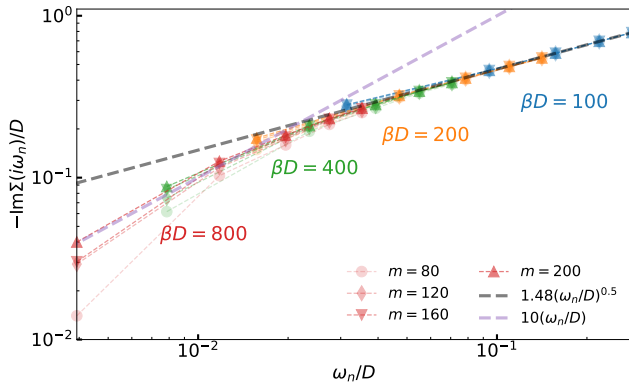


Fig. E.2. Bond dimension convergence for the degenerate three-orbital model at various temperatures using the same parameters set as Fig. E.1.

- 
- [1] W. Metzner and D. Vollhardt, *Phys. Rev. Lett.* **62**, 324 (1989).
- [2] A. Georges and W. Krauth, *Phys. Rev. Lett.* **69**, 1240 (1992).
- [3] A. Georges, G. Kotliar, W. Krauth, and M. J. Rozenberg, *Rev. Mod. Phys.* **68**, 13 (1996).
- [4] M. Imada, A. Fujimori, and Y. Tokura, *Rev. Mod. Phys.* **70**, 1039 (1998).
- [5] G. Kotliar and D. Vollhardt, *Phys. Today* **57**, 53 (2004).
- [6] G. Kotliar, S. Y. Savrasov, K. Haule, V. S. Oudovenko, O. Parcollet, and C. A. Marianetti, *Rev. Mod. Phys.* **78**, 865 (2006).
- [7] A. Georges, L. d. Medici, and J. Mravlje, *Annu. Rev. Condens. Matter Phys.* **4**, 137 (2013).
- [8] E. Gull, A. J. Millis, A. I. Lichtenstein, A. N. Rubtsov, M. Troyer, and P. Werner, *Rev. Mod. Phys.* **83**, 349 (2011).
- [9] M. Ulmke, V. Janiš, and D. Vollhardt, *Phys. Rev. B* **51**, 10411 (1995).
- [10] A. N. Rubtsov, V. V. Savkin, and A. I. Lichtenstein, *Phys. Rev. B* **72**, 035122 (2005).
- [11] P. Werner, A. Comanac, L. de' Medici, M. Troyer, and A. J. Millis, *Phys. Rev. Lett.* **97**, 076405 (2006).
- [12] P. Werner and A. J. Millis, *Phys. Rev. B* **74**, 155107 (2006).
- [13] E. Gull, P. Werner, O. Parcollet, and M. Troyer, *Europhysics Letters* **82**, 57003 (2008).
- [14] M. Caffarel and W. Krauth, *Phys. Rev. Lett.* **72**, 1545



- (1994).
- [15] G. Sangiovanni, A. Toschi, E. Koch, K. Held, M. Capone, C. Castellani, O. Gunnarsson, S.-K. Mo, J. W. Allen, H.-D. Kim, A. Sekiyama, A. Yamasaki, S. Suga, and P. Metcalf, *Phys. Rev. B* **73**, 205121 (2006).
- [16] M. Capone, L. de' Medici, and A. Georges, *Phys. Rev. B* **76**, 245116 (2007).
- [17] E. Koch, G. Sangiovanni, and O. Gunnarsson, *Phys. Rev. B* **78**, 115102 (2008).
- [18] D. Zgid, E. Gull, and G. K.-L. Chan, *Phys. Rev. B* **86**, 165128 (2012).
- [19] C. Lin and A. A. Demkov, *Phys. Rev. B* **88**, 035123 (2013).
- [20] Y. Lu, M. Höppner, O. Gunnarsson, and M. W. Haverkort, *Phys. Rev. B* **90**, 085102 (2014).
- [21] A. Amaricci, L. Crippa, A. Scazzola, F. Petocchi, G. Mazza, L. de Medici, and M. Capone, *Computer Physics Communications* **273**, 108261 (2022).
- [22] K. G. Wilson, *Rev. Mod. Phys.* **47**, 773 (1975).
- [23] R. Bulla, T. A. Costi, and T. Pruschke, *Rev. Mod. Phys.* **80**, 395 (2008).
- [24] R. Bulla, *Phys. Rev. Lett.* **83**, 136 (1999).
- [25] R. Bulla, T. A. Costi, and D. Vollhardt, *Phys. Rev. B* **64**, 045103 (2001).
- [26] R. Bulla, H.-J. Lee, N.-H. Tong, and M. Vojta, *Phys. Rev. B* **71**, 045122 (2005).
- [27] T. Pruschke, R. Bulla, and M. Jarrell, *Phys. Rev. B* **61**, 12799 (2000).
- [28] F. B. Kugler, M. Zingl, H. U. R. Strand, S.-S. B. Lee, J. von Delft, and A. Georges, *Phys. Rev. Lett.* **124**, 016401 (2020).
- [29] F. B. Kugler, *Phys. Rev. B* **105**, 245132 (2022).
- [30] S. R. White, *Phys. Rev. Lett.* **69**, 2863 (1992).
- [31] S. R. White, *Phys. Rev. B* **48**, 10345 (1993).
- [32] U. Schollwöck, *Rev. Mod. Phys.* **77**, 259 (2005).
- [33] U. Schollwöck, *Ann. Phys.* **326**, 96 (2011).
- [34] K. A. Hallberg, *Adv. Phys.* **55**, 477 (2006).
- [35] D. J. García, K. Hallberg, and M. J. Rozenberg, *Phys. Rev. Lett.* **93**, 246403 (2004).
- [36] C. Raas, G. S. Uhrig, and F. B. Anders, *Phys. Rev. B* **69**, 041102(R) (2004).
- [37] A. Holzner, A. Weichselbaum, and J. von Delft, *Phys. Rev. B* **81**, 125126 (2010).
- [38] M. Ganahl, P. Thunström, F. Verstraete, K. Held, and H. G. Evertz, *Phys. Rev. B* **90**, 045144 (2014).
- [39] M. Ganahl, M. Aichhorn, H. G. Evertz, P. Thunström, K. Held, and F. Verstraete, *Phys. Rev. B* **92**, 155132 (2015).
- [40] F. A. Wolf, I. P. McCulloch, and U. Schollwöck, *Phys. Rev. B* **90**, 235131 (2014).
- [41] F. A. Wolf, I. P. McCulloch, O. Parcollet, and U. Schollwöck, *Phys. Rev. B* **90**, 115124 (2014).
- [42] F. A. Wolf, A. Go, I. P. McCulloch, A. J. Millis, and U. Schollwöck, *Phys. Rev. X* **5**, 041032 (2015).
- [43] D. Bauernfeind, M. Zingl, R. Triebl, M. Aichhorn, and H. G. Evertz, *Phys. Rev. X* **7**, 031013 (2017).
- [44] N.-O. Linden, M. Zingl, C. Hubig, O. Parcollet, and U. Schollwöck, *Phys. Rev. B* **101**, 041101 (2020).
- [45] X. Cao, Y. Lu, P. Hansmann, and M. W. Haverkort, *Phys. Rev. B* **104**, 115119 (2021).
- [46] S. R. White, *Phys. Rev. Lett.* **102**, 190601 (2009).
- [47] E. M. Stoudenmire and S. R. White, *New Journal of Physics* **12**, 055026 (2010).
- [48] M. Binder and T. Barthel, *Phys. Rev. B* **95**, 195148 (2017).
- [49] A. E. Feiguin and S. R. White, *Phys. Rev. B* **72**, 220401 (2005).
- [50] M. Zwolak and G. Vidal, *Phys. Rev. Lett.* **93**, 207205 (2004).
- [51] F. Verstraete, J. J. García-Ripoll, and J. I. Cirac, *Phys. Rev. Lett.* **93**, 207204 (2004).
- [52] J. Hauschild, E. Leviatan, J. H. Bardarson, E. Altman, M. P. Zaletel, and F. Pollmann, *Phys. Rev. B* **98**, 235163 (2018).
- [53] J. Chen and E. M. Stoudenmire, *Phys. Rev. B* **101**, 195119 (2020).
- [54] C.-M. Chung and U. Schollwöck, arxiv (2019), arXiv:1910.03329 [cond-mat.str-el].
- [55] D. Bauernfeind, X. Cao, E. M. Stoudenmire, and O. Parcollet, *Phys. Rev. B* **105**, 195107 (2022).
- [56] D. Bauernfeind, R. Triebl, M. Zingl, M. Aichhorn, and H. G. Evertz, *Phys. Rev. B* **97**, 115156 (2018).
- [57] J. Haegeman, J. I. Cirac, T. J. Osborne, I. Pižorn, H. Verschelde, and F. Verstraete, *Phys. Rev. Lett.* **107**, 070601 (2011).
- [58] J. Haegeman, C. Lubich, I. Oseledets, B. Vandereycken, and F. Verstraete, *Phys. Rev. B* **94**, 165116 (2016).
- [59] D. Bauernfeind and M. Aichhorn, *SciPost Phys.* **8**, 024 (2020).
- [60] M. Yang and S. R. White, *Phys. Rev. B* **102**, 094315 (2020).
- [61] M. Fishman, S. R. White, and E. M. Stoudenmire, *SciPost Phys. Codebases* , 4 (2022).
- [62] M. Fishman, S. R. White, and E. M. Stoudenmire, *SciPost Phys. Codebases* , 4 (2022).
- [63] J. Kaye, K. Chen, and O. Parcollet, *Phys. Rev. B* **105**, 235115 (2022).
- [64] P. Seth, I. Krivenko, M. Ferrero, and O. Parcollet, *Computer Physics Communications* **200**, 274–284 (2016).
- [65] O. Parcollet, M. Ferrero, T. Ayrál, H. Hafermann, I. Krivenko, L. Messio, and P. Seth, *Computer Physics Communications* **196**, 398 (2015).
- [66] A. P. Mackenzie and Y. Maeno, *Rev. Mod. Phys.* **75**, 657 (2003).
- [67] Y. Maeno, H. Hashimoto, K. Yoshida, S. Nishizaki, T. Fujita, J. Bednorz, and F. Lichtenberg, *nature* **372**, 532 (1994).
- [68] A. P. Mackenzie, T. Scaffidi, C. W. Hicks, and Y. Maeno, *npj Quantum Materials* **2**, 40 (2017).
- [69] X. Deng, K. M. Stadler, K. Haule, A. Weichselbaum, J. von Delft, and G. Kotliar, *Nature communications* **10**, 2721 (2019).
- [70] J. Mravlje, M. Aichhorn, T. Miyake, K. Haule, G. Kotliar, and A. Georges, *Phys. Rev. Lett.* **106**, 096401 (2011).
- [71] A. Tamai, M. Zingl, E. Rozbicki, E. Cappelli, S. Riccò, A. de la Torre, S. McKeown Walker, F. Y. Bruno, P. D. C. King, W. Meevasana, M. Shi, M. Radović, N. C. Plumb, A. S. Gibbs, A. P. Mackenzie, C. Berthod, H. U. R. Strand, M. Kim, A. Georges, and F. Baumberger, *Phys. Rev. X* **9**, 021048 (2019).
- [72] H. U. R. Strand, M. Zingl, N. Wentzell, O. Parcollet, and A. Georges, *Phys. Rev. B* **100**, 125120 (2019).
- [73] M. Kim, J. Mravlje, M. Ferrero, O. Parcollet, and A. Georges, *Phys. Rev. Lett.* **120**, 126401 (2018).
- [74] M. W. Haverkort, I. S. Elfimov, L. H. Tjeng, G. A. Sawatzky, and A. Damascelli, *Phys. Rev. Lett.* **101**, 026406 (2008).
- [75] P. Blaha, K. Schwarz, G. K. Madsen, D. Kvasnicka,

- J. Luitz, *et al.*, An augmented plane wave+ local orbitals program for calculating crystal properties (2001).
- [76] P. Blaha, K. Schwarz, F. Tran, R. Laskowski, G. K. H. Madsen, and L. D. Marks, *J. Chem. Phys.* **152**, 074101 (2020), <https://doi.org/10.1063/1.5143061>.
- [77] A. A. Mostofi, J. R. Yates, G. Pizzi, Y.-S. Lee, I. Souza, D. Vanderbilt, and N. Marzari, *Comput. Phys. Commun.* **185**, 2309 (2014).
- [78] G. Zhang, E. Gorelov, E. Sarvestani, and E. Pavarini, *Phys. Rev. Lett.* **116**, 106402 (2016).
- [79] The quasiparticle weight  $Z$  is determined by fitting a polynomial of 4th order to the lowest 6 points of the Matsubara self-energies.
- [80] J. Karp, M. Bramberger, M. Grundner, U. Schollwöck, A. J. Millis, and M. Zingl, *Phys. Rev. Lett.* **125**, 166401 (2020).
- [81] A. Hunter, S. Beck, E. Cappelli, F. Margot, M. Straub, Y. Alexanian, G. Gatti, M. D. Watson, T. K. Kim, C. Cacho, N. C. Plumb, M. Shi, M. Radović, D. A. Sokolov, A. P. Mackenzie, M. Zingl, J. Mravlje, A. Georges, F. Baumberger, and A. Tamai, *Phys. Rev. Lett.* **131**, 236502 (2023).
- [82] A. Wietek, Y.-Y. He, S. R. White, A. Georges, and E. M. Stoudenmire, *Phys. Rev. X* **11**, 031007 (2021).
- [83] A. Wietek, R. Rossi, F. Šimkovic, M. Klett, P. Hansmann, M. Ferrero, E. M. Stoudenmire, T. Schäfer, and A. Georges, *Phys. Rev. X* **11**, 041013 (2021).
- [84] C. Feng, E. M. Stoudenmire, and A. Wietek, *Phys. Rev. B* **107**, 205150 (2023).
- [85] B.-B. Chen, L. Chen, Z. Chen, W. Li, and A. Weichselbaum, *Phys. Rev. X* **8**, 031082 (2018).
- [86] A. Liebsch and H. Ishida, *Journal of Physics: Condensed Matter* **24**, 053201 (2011).
- [87] D. Sénéchal, *Physical Review B* **81**, 235125 (2010).
- [88] C. Mejuto-Zaera, L. Zepeda-Núñez, M. Lindsey, N. Tubman, B. Whaley, and L. Lin, *Phys. Rev. B* **101**, 035143 (2020).
- [89] P. Werner, E. Gull, M. Troyer, and A. J. Millis, *Phys. Rev. Lett.* **101**, 166405 (2008).
- [90] P. Werner, E. Gull, and A. J. Millis, *Phys. Rev. B* **79**, 115119 (2009).